


## ORIGINAL RESEARCH

# Dual- and triple-passband coupled-complementary FSSs based on the four-arms star geometry

Deisy F. Mamedes<sup>1</sup>  | Jens Bornemann<sup>1</sup> | Alfredo Gomes Neto<sup>2</sup> |  
Sérgio L. M. Sales Filho<sup>2</sup>

<sup>1</sup>Department of Electrical and Computer Engineering, University of Victoria, Victoria, British Columbia, Canada

<sup>2</sup>Department of Electrical Engineering, Federal Institute of Paraíba, João Pessoa, Paraíba, Brazil

## Correspondence

Deisy F. Mamedes.

Email: [mamedes@ieee.org](mailto:mamedes@ieee.org)

## Abstract

The authors propose a system of closely coupled-complementary frequency-selective surfaces (FSSs) based on the four-arms star geometry with dual- and triple-passbands responses for 5G applications. Four complementary structure configurations are presented, and depending on the chosen configuration, the structure can create two or three transmission bands in one or both polarisations of the electromagnetic waves. The designed FSSs are compact and have stable behaviour at different incident angles. The complementary FSS passes signals around 2.6 and 6.2 GHz, and a structural offset allows the transmission at a third frequency (4.2 GHz). To validate the proposed designs, four prototypes are fabricated and measured. Numerical and experimental characterisations are in good agreement.

## KEYWORDS

5G mobile communication, electromagnetic induction, electromagnetic wave scattering, frequency selective surfaces, multilayers

## 1 | INTRODUCTION

The fifth generation (5G) wireless communication systems provide high speed and good quality transmission, while supporting a wide variety of data usage volumes. Modern communication systems face the existence of various kinds of interference signals and limited spectrum resources. Systems that can serve users with multiple bands at the same time, while blocking unwanted signals have become desirable. Frequency-selective surfaces (FSSs) with multi-band characteristics have appeared as a solution to be incorporated in these systems to meet their stringent requirements.

FSSs are planar periodic structures, formed by patch (conductive) or slot (aperture) elements etched on a dielectric substrate. Depending on the type of the chosen element, FSSs can have total reflection (patch) or transmission (slot) of the incident electromagnetic (EM) waves, providing filtering properties [1, 2]. FSSs have been widely used in the microwave and

millimetre-wave ranges, in applications, such as sub-reflectors of multiband antennas [3, 4], polarisation converters [5, 6], radar cross-section reduction [7, 8], and absorbers [9, 10].

When the periodic arrays of patch- and slot-type elements have identical shape, they present a complementary response, that is, the specular reflection of EM waves for one array is equal to the transmission of EM waves of its complementary one. This arrangement follows Babinet's principle which states that the sum of the wave transmitted through a screen with an aperture and the wave transmitted through a complementary structure is equal to the wave transmitted when no screen is present [1, 11]. Note that Babinet's principle is for free-standing structures, that is, complementary FSSs (CFSSs) are not purely Babinet's complement because of the presence of a dielectric (for mechanical purposes) between the patch and slot arrays, but the general concept still applies [12]. The two metallic layers combined in CFSSs will experience an interaction of transmission and reflection characteristics of each

**Abbreviations:** 5G, fifth generation; AS, angular stability; CFSS, complementary frequency-selective surface; EIT, electromagnetically induced transparency; EM, electromagnetic; FSS, frequency-selective surface; PI, polarisation insensitive; RFD, resonant frequency deviation; TE, transverse electric; TL, transmission loss; TM, transverse magnetic.

This is an open access article under the terms of the [Creative Commons Attribution-NonCommercial-NoDerivs](https://creativecommons.org/licenses/by-nc-nd/4.0/) License, which permits use and distribution in any medium, provided the original work is properly cited, the use is non-commercial and no modifications or adaptations are made.

© 2024 The Authors. *IET Microwaves, Antennas & Propagation* published by John Wiley & Sons Ltd on behalf of The Institution of Engineering and Technology.

individual layer, due to a strong EM coupling between the layers, leading to the CFSS response.

Ref. [13] proposes an angular stable dual-band FSS with anchor-shaped elements with different structural parameters along the  $x$ -axis alternately within a hexagonal wire grid mounted on a single-layer dielectric substrate. The FSS operates its two passbands in the Ku-band. Although the structure only uses one metal and one dielectric layer, the geometry is complex to design. The operating frequencies are stable under oblique incidence, but there is a deterioration of the first transmission band by about 50% at an angle of incidence of  $60^\circ$ , and the structure is polarisation sensitive.

Ref. [14] presents an antipodal F-type FSS with multi-band characteristics. The structure consists of a dielectric substrate with double metallisation. The top layer is formed by four rotated F-type resonators, another set of them scaled down placed in the inner side of this layer, and a square loop surrounding all resonators. The bottom layer is formed by antipodal all F-type resonators. The structure operates at 2.4, 5.2 and 5.9 GHz with measured results for normal incidence ( $\theta = 0^\circ$ ) and stable performance for oblique incidence up to  $60^\circ$  for numerical results with maximum resonant frequency deviation (RFD) of 1.6%.

A dual-band FSS, operating in the Ku-band, based on two circular patches and a circular coupling aperture, whose elements have different sizes, is presented in Ref. [15]. The structure is composed of three metallic and two dielectric layers, with unit cell dimensions of about half a wavelength, which makes the proposed FSS large and bulky. The results show low attenuation in the rejection band (approx.  $-18$  dB) between the two passbands.

A miniaturised dual-band FSS with frequencies of operation in X- and Ka-band is proposed in Ref. [16], where a cascade system of two-dimensional periodic arrays of double square loops and an array of wire grids are implemented to achieve small element size. The proposed structure is composed of three metal and two dielectric layers that act as a spatial dual-band microwave filter with large band separation.

Ref. [17] proposes a multi-layered FSS with multi-band response and polarisation dependence. The structure is composed of three layers of metal and two layers of dielectric substrate. The design consists of a metal square aperture element between two identical asymmetric Jerusalem cross patches, resulting in a miniaturised structure. It presents dual-band behaviour for the transverse electric (TE) polarisation with resonant frequencies at 7.28 and 26.94 GHz and single-band characteristics for the transverse magnetic (TM) polarisation with a resonant frequency at 11.39 GHz.

A triple-passband highly selective FSS with miniaturisation characteristics is proposed in Ref. [18]. The structure consists of a multi-layer combination of three metal layers separated by two dielectric substrates. The top and bottom layers have the same pattern which is composed of a meandered cross slot and four edge slots. The middle layer is formed by metallic square loops. The three passbands are located at 20.9 GHz, 29.9, and 38.5 GHz. The out-of-band isolation between operating bands is up to 20 dB.

Ref. [19] presents an FSS with triple-passband response achieved by cascading three layers of periodic arrays. The top and bottom layers are composed of gridded-double square loop elements, and the middle layer is composed of double square loops. The results show a wide out-of-band rejection between the adjacent passbands provided by multiple transmission zeros. As the angle of incidence increases, the attenuation reduces by about 20 dB for an incidence of  $60^\circ$ .

A dual-band FSS with passband response is developed in Ref. [20]. The FSS is composed of two metal-based square patch layers at the two ends and one aperture type layer in the middle, separated by two dielectric substrates. The structure exhibits two passbands at 2.5 and 5.5 GHz. The design is polarisation sensitive, and the authors only exploited the TE polarisation, showing it to be stable for oblique incidence up to  $45^\circ$ .

A single-layer triple-passband FSS with less sensitivity to changes in the angle of incidence is proposed in Ref. [21]. The structure's element is formed by a combination of a square patch, a U-shaped slot, a replicated T-shaped slot and a rectangular-shaped slot, which achieves triple-band response. Although the structure uses only one metallic layer, the size of the unit cell is large, and the design of its elements is complex.

Ref. [22] presents a dual-band FSS with bandpass characteristics based on the Matryoshka-like geometry. The single-layer structure consists of convoluted slot-type elements that offer miniaturisation characteristics. The FSS response is polarisation independent with good angular stability up to  $45^\circ$ .

A varactor-based polarisation-insensitive dual-passband FSS with independent tunability is implemented in Ref. [23]. The structure is formed by two metallic layers in a 2.5-D configuration. The top one evolved from a classical cross-shaped structure surrounded by an inductive grid, including the centre cross structure and four U-shaped metallic lines with corresponding T-shaped metallic lines. The biasing network is found in the bottom layer. A shunted substrate integrated waveguide cavity-like structure is designed, connecting the top and bottom layers, to realise electromagnetic isolation and serve as the dc ground for varactors to simplify the dc bias feed network.

In this work, dual- and triple-passbands FSSs are proposed for 5G applications using complementary structures. Double- and single-metallic layered structures, supported by only a single substrate, represent closely coupled-complementary FSSs inspired by Babinet's principle. The proposed CFSS uses a non-traditional geometry that has a very easy design process and a simple fabrication process, when compared to some published complementary structures [11, 24–26]. The element's geometry and filtering mechanism are presented, showing that the operating frequencies can be adjusted independently. In addition, offset-based structures are proposed as well, and they were fabricated to validate their design, where the Electromagnetically Induced Transparency (EIT) effect is applied to create an extra passband. Measurements of the transmission coefficients, including normal and oblique incidence, are presented, showing good agreement with simulated results.

This paper is organised as follows. The design procedure of the element used for the patch- and slot-type unit cells is described in Section 2. The complementary structures and three other derived configurations are presented in Section 3. In Section 4, the numerical and experimental results are presented to validate the proposed designs, and the conclusions are presented in Section 5.

## 2 | SINGLE-LAYER FSS ANALYSIS AND DESIGN

This section presents the design and analysis of a unit-cell FSS based on the four-arms star geometry with a patch-type element and its complementary one, individually, on single-layer substrate. The numerical characterisations of all structures are obtained through the commercial software package CST Microwave Studio. The simulated results for all structures are performed considering the single unit cell for less computational effort when compared to the simulation for the FSS panel. We determined the difference between these two simulations to be less than 0.35%. The dielectric substrate considered in the simulation has  $\epsilon_r = 4.4$ , thickness of 1.0 mm, and loss tangent of 0.025.

### 2.1 | Four-arms star patch-type FSS

The first structure is the four-arms star patch-type element so that in this case, the inside of the element has metallic filling. Figure 1a illustrates the unit cell with this element, including its parameters. The following steps are performed to achieve this configuration: the unit cell dimension is defined as  $p$ , and then, a rectangular patch is designed as  $a$ , where the arms are shaped. From the edges, lines that cross the rectangular patch with  $b$  are drawn, and the star geometry is achieved with pointed arms. A small square patch of width  $s$  is etched at the centre to connect all four arms. Finally, the outside of the element is detached from the metallic surface, and the four-arms star unit cell is completed. Refs. [6, 27] present the initial equations to design and determine the resonant frequency for the FSS using this geometry. The dimensions of the structure are  $p_p = 17$  mm,  $a_p = 15.4$  mm,  $s_p = 2$  mm and  $b_p = 1.5$  mm. The numerical characterisation of the four-arms star patch-type FSS is shown in Figure 2 (blue curve), with resonant frequency at 5.24 GHz and characteristics as a stop-band filter.

### 2.2 | Four-arms star slot-type FSS

The design procedure of the four-arms star slot-type is similar to patch one, except that in this case, the inside of the element is detached from the metallic surface. Figure 1b shows the slot unit cell with its parameters.

The design process of the four-arms star slot-type FSS follows the same concept used for a cross-dipole element [28,

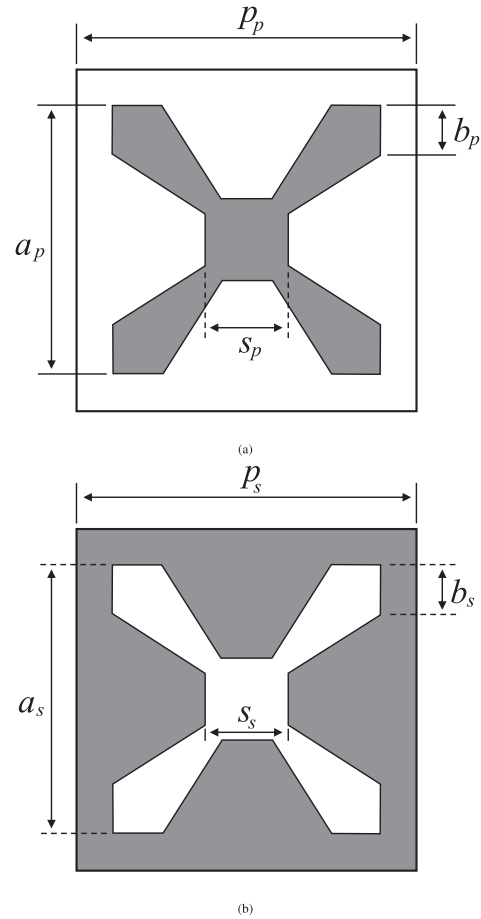


**FIGURE 1** Geometry and parameters of single-layer (a) patch-type and (b) slot-type FSSs.

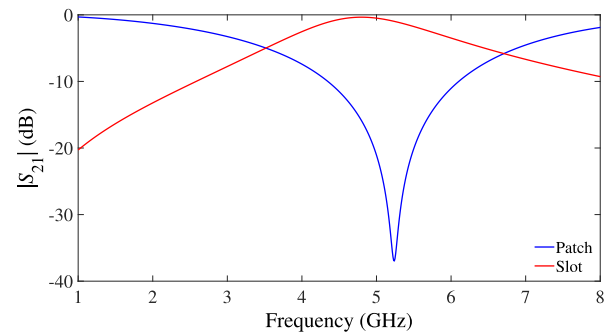


**FIGURE 2** Numerical results of patch-type and slot-type elements FSSs.

29], where the length of the arms is set to half wavelength; then, the first resonant frequency can be estimated as follows:

$$f_{\text{slot}}(\text{GHz}) = \frac{0.3}{2a_s \sqrt{\epsilon_{r\text{eff}}}} \quad (1)$$

Note that the design considers a dielectric slab added to the array; thus, the resonant frequency is shifted when compared to the free-standing structure. The frequency is shifted with the

factor  $\sqrt{\epsilon_{r_{\text{eff}}}}$  as shown in the above equation. Ref. [30] presents an interpolating formula that fits the variation of the effective permittivity

$$\epsilon_{r_{\text{eff}}} = \epsilon_r + (\epsilon_r - 1) \left[ \frac{-1}{e^{\frac{10b}{p_s} N}} \right] \quad (2)$$

which considers the dielectric permittivity and thickness of the substrate  $h$ , periodicity  $p_s$ , and the exponential factor,  $N$ , of the unit cell filling. For the geometry proposed, the value of  $N$  is 3.8.

In this design, the structure parameters have the same value as the patch-type one, that is,  $p_s = p_p$ ,  $a_s = a_p$ ,  $s_s = s_p$  and  $b_s = b_p$ . As expected, the frequency response of the slot-type FSS has a band-pass behaviour with a resonant frequency at 4.82 GHz (Figure 2, red curve), with a difference of 8% compared to the resonant frequency of the patch-type FSS. The difference between the reflection coefficient of the patch element and the transmission coefficient of its complementary one is due to the fact that the structures are not freestanding. A dielectric substrate is used for mechanical support, and its parameters affect the frequency response of the arrays, shifting their resonant frequency as established in Equation (1). If the dielectric slab is removed from both structures, they will exhibit the same resonant frequency.

### 3 | COMPLEMENTARY FSS ANALYSIS AND DESIGN

This section describes the design procedure of the CFSS, which combines the structures presented in the previous section. Four complimentary configurations are derived from combinations of the patch- and slot-type FSSs.

#### 3.1 | CFSS configuration

The complementary structure is achieved by designing the patch and slot elements using identical geometry shape and dimensions, and these elements are spaced by a medium. Figure 3 illustrates the three-dimensional topology of the proposed CFSS. The medium used to separate the elements is a dielectric substrate with thickness  $h$  and dielectric constant  $\epsilon_r$ . The top layer of the substrate is formed by the patch element, while the bottom layer carries slot one. In this work, the CFSS was designed with the same dimensions used for the individual FSSs presented in Section 2.

##### 3.1.1 | CFSS working principle

The patch and slot FSSs have complementary responses as demonstrated in Section 2. This occurs because the patch element behaves as a series LC circuit, providing a stopband

filter response, while the slot element has characteristics of a parallel LC circuit with passband filter response [28]. When these two elements are stacked on a substrate with double metallic layers, for example, as illustrated in Figure 3, the equivalent circuit for the proposed CFSS combines the equivalent circuits of the patch and slot elements as shown in Figure 4, which predicts that this structure will present two transmission maxima ( $f_{p1}$  and  $f_{p2}$ ) separated by a transmission zero ( $f_z$ ) [31–33] (Figure 6). Note that an impedance  $Z_d$  is added to account for the mutual coupling between the metallic layers. The discrete values of the equivalent circuit model for this structure are  $L_p = 39.44$  pH,  $C_p = 36$  pF,  $L_s = 36$  pH and  $C_s = 46.59$  pF.

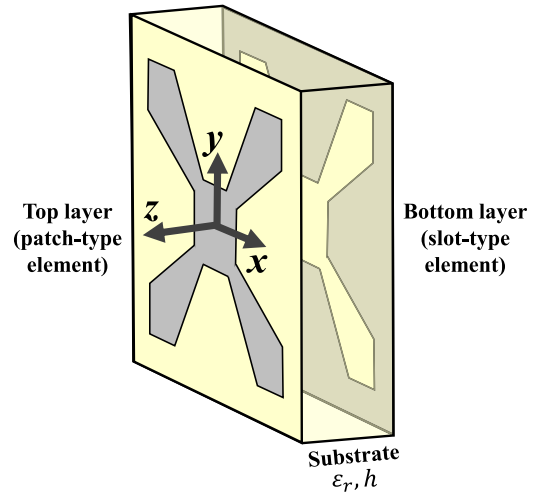


FIGURE 3 CFSS structuring.

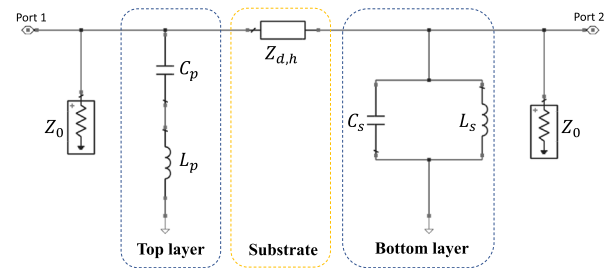


FIGURE 4 CFSS equivalent circuit.

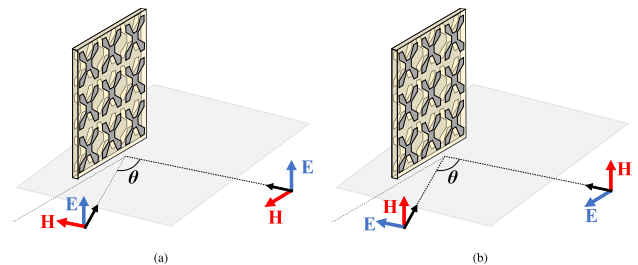
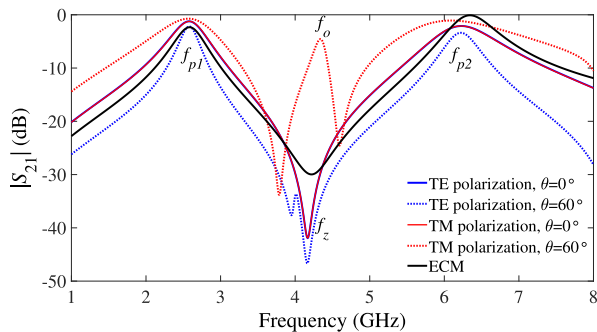


FIGURE 5 Polarizations of the (a) TE and (b) TM incident wave on the complementary FSS.



A TE (Figure 5a) and TM (Figure 5b) polarised wave arrives at the complementary FSS at normal ( $\theta = 0^\circ$ ) and oblique ( $\theta \neq 0^\circ$ ) incidence. The simulated transmission spectra of the complementary FSS considering these incidences are plotted in Figure 6 and compared with the result of the equivalent circuit. The corresponding spectrum exhibits two transmission maxima ( $f_{p1}$  and  $f_{p2}$ ), as exploited above, and a transmission null ( $f_z$ ) at normal incidence for both polarisations. When the angle of the incident wave is increased, the horizontal E-field probes a break in the symmetry of the two resonators, making the transmission null to become a transmission maximum ( $f_o$ ). This phenomenon is known as Electromagnetically Induced Transparency (EIT)-like effect. The destructive interference at a particular frequency cancels the resonance effect due to the antiparallel currents of the two closely placed resonators. To further understand the physical mechanism, the surface current on each metal layer at the resonant frequencies are shown in



**FIGURE 6** Theoretical and simulated transmission spectra of proposed CFSS for TE and TM polarisation at  $\theta = 0^\circ$  and  $\theta = 60^\circ$ .

Figure 7. Note that all currents are plotted with a common scale of 0–200 A/m.

This first proposed structure exhibits the same response at normal incidence for TE and TM polarisation. Thus, the surface current of this structure is plotted when the E-field of the incident wave is vertically polarised (Figures 7a–c). The surface current of the two transmission maxima is demonstrated in Figure 7a,b, suggesting that the passbands are formed by the edges of the arms of the slot element and the centre of the patch element so that the current maxima of opposite directions appear around the corner of this spot in each element. Figure 7c shows the surface current of the stopband at  $f_z$ , and there is no area with dense current distribution, which means the electromagnetic wave reflects through the FSS. As mentioned above, a transparency window is seen at oblique incidence for TM polarisation. To sort out the causes for  $f_o$ , we check the current distribution due to horizontally polarised oblique ( $\theta = 60^\circ$ ) incidence (Figure 7d). The current distribution in this scenario is similar to the ones found for  $f_{p1}$  and  $f_{p2}$  for the slot element, while in the patch element, the current maximum happens on one of each edges of the arms. This happened because in this condition the geometry symmetry is broken, leading to the excitation of the EIT-like effect by the coupling of the resonators modes.

A parametric analysis served to evaluate the influence of the substrate thickness  $h$  and dielectric permittivity  $\epsilon_r$ . Figure 8a presents the results considering  $\epsilon_r = 4.4$  and varying the substrate thickness of  $h = 0.25, 0.5, 0.75, 1.00, 1.50, 3.00$  and  $6.00$  mm. The increase in the parameter  $h$  leads to the increase of the insertion loss at the desired frequencies. This effect is due to the degradation of coupling between the patch and slot elements. Note that the substrate thickness does not affect the resonant

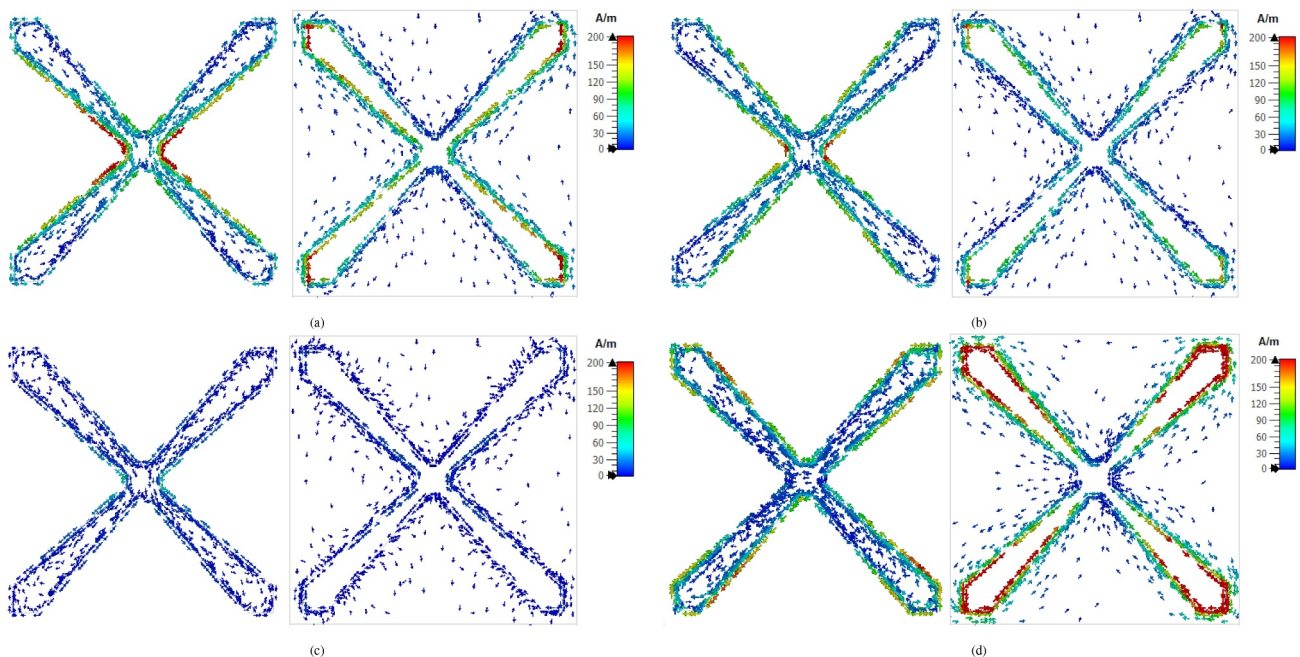


**FIGURE 7** Surface currents on CFSS #1 with vertical polarised normal incidence at (a)  $f_{p1}$ , (b)  $f_{p2}$  and (c)  $f_z$ , and with horizontal polarised oblique ( $\theta = 60^\circ$ ) incidence at (d)  $f_o$ .

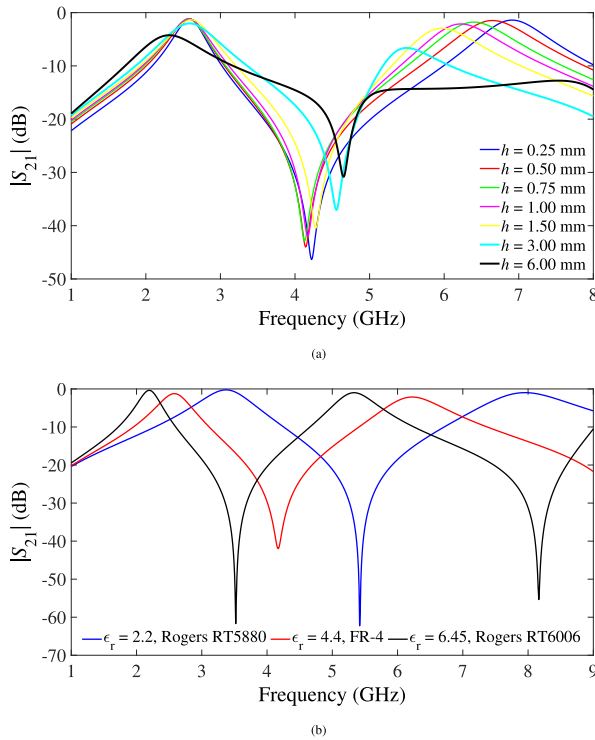


**FIGURE 8** Comparison of frequency response (a) as a function of substrate thickness of CFSS with  $\epsilon_r = 4.4$ , and (b) as a function of dielectric permittivity of CFSS with  $h = 1$  mm.

frequency of the first passband, only its bandwidth, because the substrate thickness is much smaller than the equivalent wavelength, but it does affect the second pass-band frequency. As  $h$  increases, the second passband moves closer to the first one, until the separation of the elements causes its decoupling, making the second passband disappear completely and the FSS complementarity breaks down. The effect of the dielectric permittivity can be seen in Figure 8b. In this case, three substrate materials were considered, each of them has a different dielectric permittivity, with the substrate thickness set to  $h = 1$  mm. The materials analysed are Rogers RT5880 with  $\epsilon_r = 2.2$  and loss tangent ( $\tan\delta$ ) of 0.009, FR-4 fibre-glass with  $\epsilon_r = 4.4$  and  $\tan\delta = 0.025$ , and Rogers RT6006 with  $\epsilon_r = 6.45$  and  $\tan\delta = 0.0027$ . As  $\epsilon_r$  increases, the resonant frequencies reduce as expected from Equation (1) and [6, 27] for the design of the single-layer structures, which governs the CFSS response, and the bandwidth for both passbands are decreased. Although the thinner substrate and Rogers' materials offer low insertion loss, the FR-4 with  $h = 1$  mm is chosen due to its low cost, commercial availability, and ease of fabrication/use.

A parametric analysis of the effect of elements' parameters on resonant frequencies and bandwidths was conducted, and the results are presented in Figure 9. The parameters  $p_p$  and  $p_s$  affect the bandwidths, whereas the increase reduces the passbands width while increasing the stopband width. When increasing  $b_p$  and  $b_s$ , they provide a complementary effect in the first passband. When  $s_p$  and  $s_s$  are increased, they exhibit a complementary effect in the second passband. The stopband is affected by  $b_p$  and  $a_s$ . The two transmission maxima are mainly

determined by  $a_p$  and  $a_s$  and can be tuned by the size of  $b_p$  and  $s_s$ . The transmission zero can be adjusted by  $b_p$  and  $b_s$ , showing a complementary effect to that of  $a_p$  and  $s_p$ .

## 3.2 | Offset CFSS configuration

To evaluate the FSS complementarity, the patch and slot elements were offset from the centre of the unit cell and its frequency response checked. In CFSS #2, a vertical offset of the elements is considered (Figure 10, left); while for CFSS #3, the elements are moved diagonally (Figure 10, right). Note that these structures have their elements with the same parameter dimension as in CFSS #1.

### 3.2.1 | Offset CFSS working principle

The main idea of offsetting the elements is to form a transmission window at normal incidence in one or both polarisations by applying the EIT-like effect. When both elements of the CFSS are offset vertically ( $y$ -direction), the E-field in the TE polarisation sees that the overall geometry is disturbed. In this scenario, a new transmission maximum ( $f_o$ ) arises at the frequency that was initially the transmission zero ( $f_z$ ) between  $f_{p1}$  and  $f_{p2}$  from the original CFSS configuration (Figure 11, solid blue curve). In the TM polarisation, the E-field does not see this change, thus maintaining almost the same response as in the original CFSS with normal incidence (Figure 11, dashed blue curve). For the CFSS with both elements offset in the diagonal orientation, a perturbation in the geometry of the unit cell is noticed by the vertical and horizontal E-field, allowing a transparency window to appear between  $f_{p1}$  and  $f_{p2}$  in both polarisations (Figure 11, solid and dashed red curves).

The induced surface current of the vertical and diagonal offset structures at  $f_o$  is demonstrated in Figure 12, considering the vertical E-field at normal incidence. The offset placement of the elements induces the anti-parallel currents, cancelling the transmission null by inducing an EIT-like effect to achieve a bandpass window in the transmission spectra. Note that the current distribution for the vertical offset at normal incidence in the TE polarisation, as shown in Figure 12a, is similar to the one found in CFSS #1 with  $\theta = 60^\circ$  in the TM polarisation (Figure 7d). Moreover, the vertical offset only offers a transmission window in one polarisation, making the structure polarisation dependent. When the diagonal offset is applied, a transparency window is achieved in both polarisations, making the structure polarisation insensitive. As shown in Figure 12b, the diagonal offset also induces an EIT-like effect, but the power in the  $f_o$  band is divided, thus increasing the transmission (insertion) loss.

## 3.3 | Single-layer quasi-CFSS configuration

To further evaluate the coupling between the elements, a fourth CFSS-based configuration is designed. In this

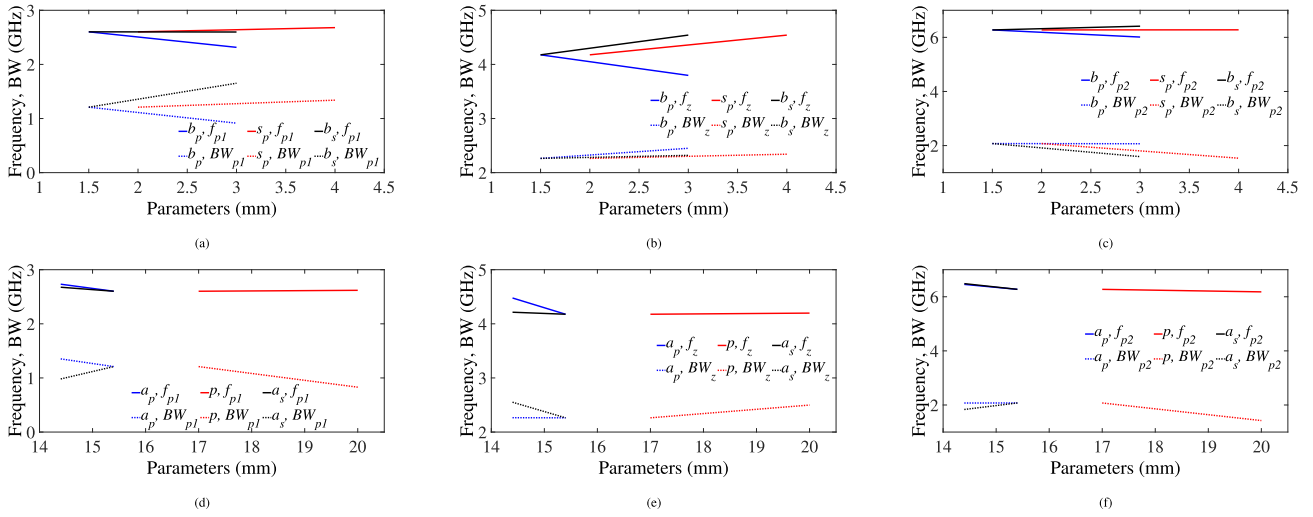


**FIGURE 9** Effect of variation in elements' parameters on resonant frequencies and bandwidths. Variation of  $b_p$ ,  $s_p$  and  $b_s$  and its effect on (a)  $f_{p1}$  and  $BW_{p1}$ , (b)  $f_z$  and  $BW_{zs}$ , (c)  $f_{p2}$  and  $BW_{p2}$ . Variation of  $a_p$ ,  $p$  and  $a_s$  and its effect on (d)  $f_{p1}$  and  $BW_{p1}$ , (e)  $f_z$  and  $BW_{zs}$ , (f)  $f_{p2}$  and  $BW_{p2}$ .

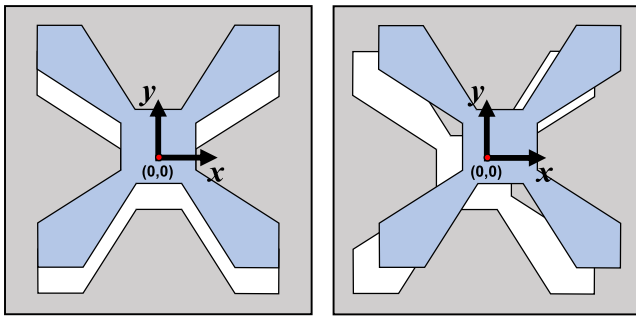


**FIGURE 10** CFSS-based configurations with vertical (CFSS #2, left) and diagonal (CFSS #3, right) offset.

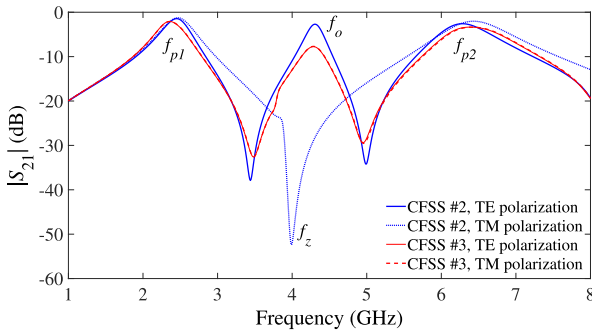


**FIGURE 11** Simulated transmission spectra of CFSS #2 and CFSS #3 for TE and TM polarisation at  $\theta = 0^\circ$ .

configuration, the substrate only has a single-metal layer, and both patch and slot elements are etched on it. The elements are complementary in shape, but not in size. The patch element's dimension remains basically the same, but the unit cell of the slot element is adjusted to dovetail all the elements. Figure 13 shows the proposed single-layer complementary-based FSS (CFSS #4).

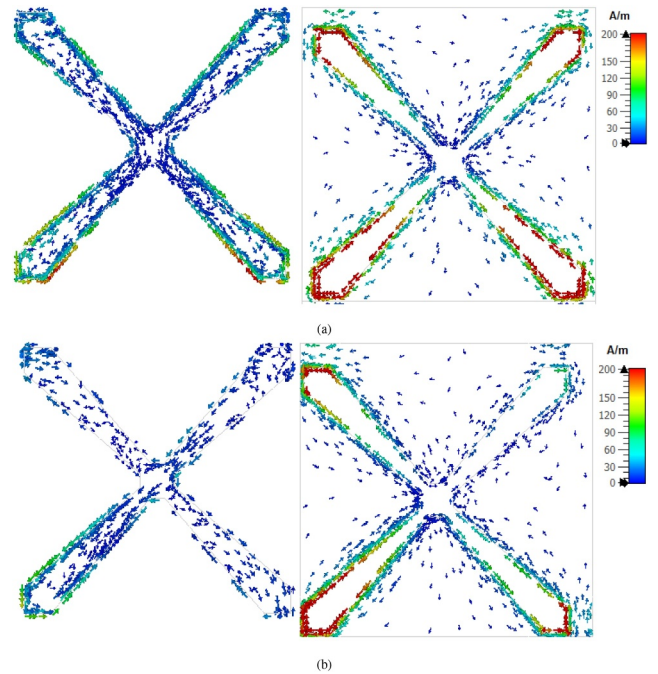


**FIGURE 12** Surface currents on (a) CFSS #2 and (b) CFSS #3 at  $f_o$  with vertical polarised normal incidence.

### 3.3.1 | Single-layered quasi-CFSS working principle

A parametric analysis is carried out to assess the influence of each element's size in the frequency response of the structure. Seven cases are analysed with different values for the parameters of the elements (Table 1), but all cases consider the same unit cell size  $p = 18$  mm and FR-4 substrate with  $h = 1$  mm.

From the results shown in Figure 14, it can be seen that each parameter differently affects the CFSS #4 response.



The first case (Case #1) shows the effect of  $a_s$  in the response of the structure, which moves  $f_{p2}$  and maintains its bandwidth, but it changes the bandwidth of the first passband to becoming more capacitive as  $a_s$  is increased. In Case #2, the size of the arms of the patch element ( $a_p$ ) is changed, which shows a similar behaviour as in Case #1 of moving  $f_{p2}$  and not altering its bandwidth, but now, the first passband becomes more inductive as  $a_p$  increases. For Case #3,  $b_p$  only affects  $f_{p1}$  and its bandwidth by moving  $f_z$  while maintaining the second passband. Case #4 changes the value of  $b_s$ , hence moves  $f_{p2}$  and adjusts the transmission zeros to change the transmission bandwidth while keeping the same rejection bandwidth. If the first passband gets narrow, the

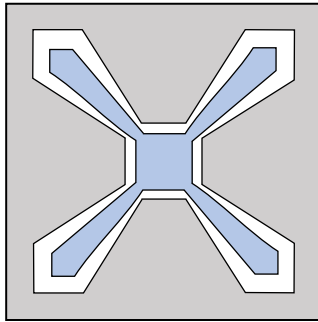


FIGURE 13 Single-layer complementary based FSS (CFSS #4).

TABLE 1 Values of CFSS#4 parameters (mm). Dimensions according to Figure 1.

	$a_p$	$a_s$	$b_p$	$b_s$	$s_p$	$s_s$
Case #1	15.5	16	1.5	5	2	3
Case #2	14.5	17	1.5	5	2	3
Case #3	15.5	17	3	5	2	3
Case #4	15.5	17	1.5	3	2	3
Case #5	15.5	17	1.5	5	2.8	3
Case #6	15.5	17	1.5	5	2	5
Case #7	15.5	17	1.5	5	2	3

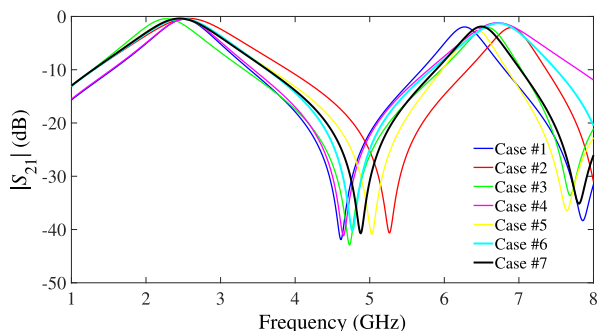


FIGURE 14 Comparison of frequency response as a function of varying CFSS #4 parameters as shown in Table 1 with unit cell size of 18 mm.

second one gets wider and vice-versa. In Case #5 and Case #6, the parameters  $s_p$  and  $s_s$  are analysed; therefore, for both cases, the first transmission resonance and its bandwidth remain untouched, while the second transmission maxima and their bandwidths change. The second passband becomes narrower if  $s_p$  is increased (more inductive) and wider if  $s_s$  is increased (more capacitive). To summarise, this analysis shows that the patch and slot elements are closely coupled and present the same characteristics as for the complementary FSS, and the bandwidths and resonant frequencies can be adjusted. The final dimensions chosen for CFSS #4 are presented in Case #7.

As to the CFSS #4, the S-parameter spectrum shown in Figure 14 indicate two passband and one stopband. Figure 15 shows the surface current at corresponding resonant frequencies. Similarly to CFSS #1, the current maxima of CFSS #4 are found at the same spots for Figure 15a,b. Again, there is no dense current distribution for  $f_z$  (Figure 15c).

## 4 | PERFORMANCE VALIDATION

Experimental characterisations of the four proposed CFSS-based configurations were performed to validate the numerical results. All prototypes were manufactured on a single-layer low-cost FR-4 fibre-glass dielectric substrate with  $\epsilon_r = 4.4$ , thickness of 1.0 mm, and  $\tan\delta = 0.025$ . Metallisation are on both sides for CFSS #1, #2 and #3 designs, and single-sided for CFSS #4. The fabricated CFSSs have  $11 \times 11$  elements and overall dimensions of  $18.7 \text{ cm} \times 18.7 \text{ cm}$  (CFSS #1, #2 and #3) and  $19.8 \text{ cm} \times 19.8 \text{ cm}$  (CFSS #4). The fabricated prototypes are presented in Figure 16. The top and bottom views of CFSS #1 are shown in Figure 16a,b, respectively, with

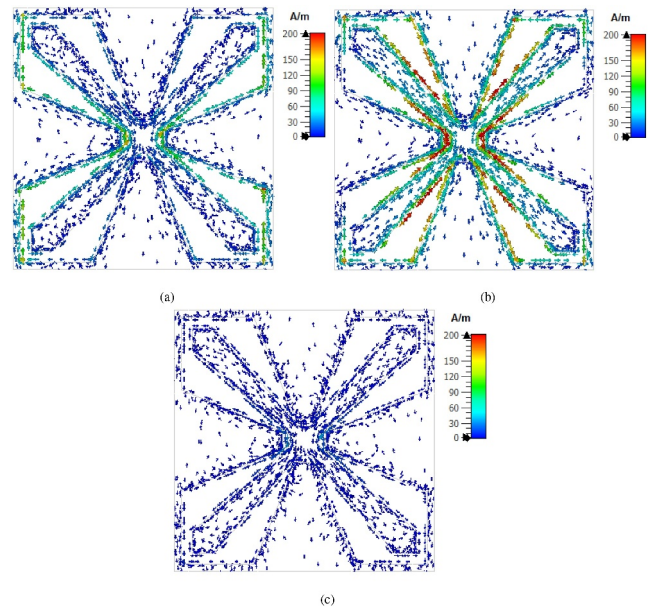
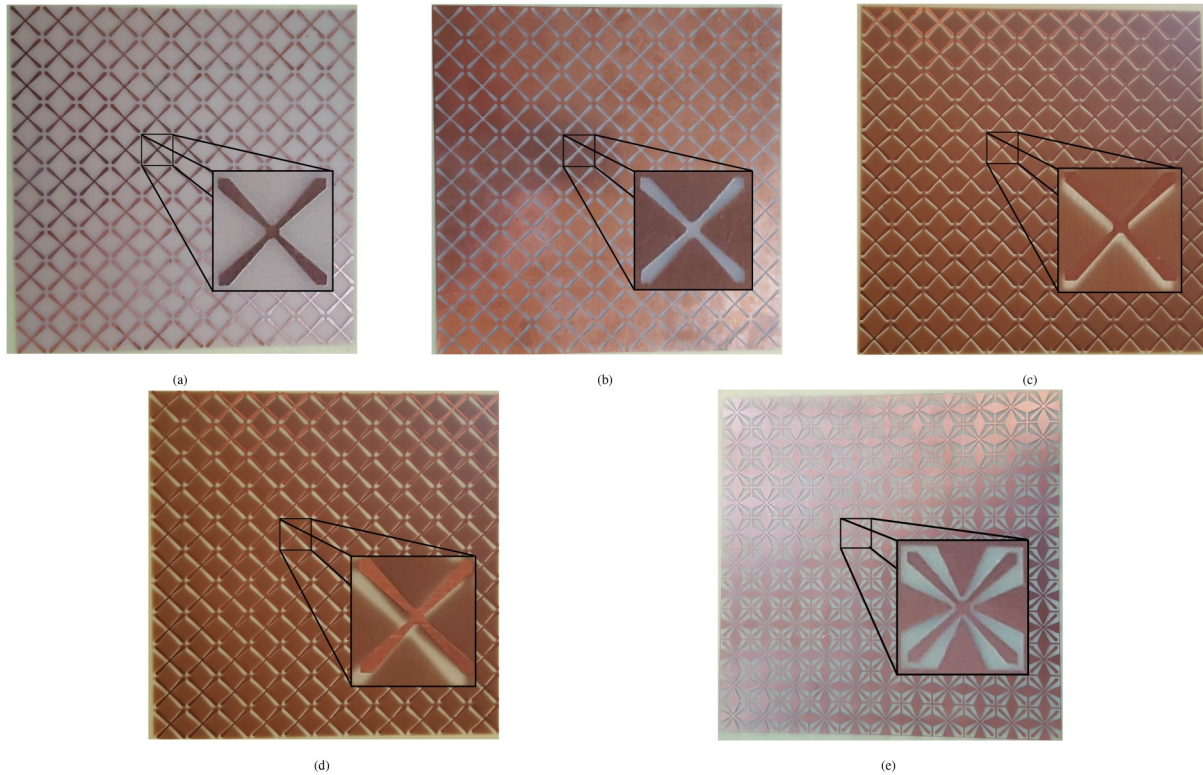


FIGURE 15 Surface currents on CFSS #4 with vertical polarised normal incidence at (a)  $f_{p1}$ , (b)  $f_{p2}$  and (c)  $f_z$ .





**FIGURE 16** Fabricated complementary structures: (a) CFSS #1 (top view, patch elements), (b) CFSS #1 (bottom view, slot elements), (c) CFSS #2 (top view), (d) CFSS #3 (top view), and (e) CFSS #4.

enlargement of the unit cell of the patch and slot elements. The structures with the vertical and diagonal offsets are illustrated in Figure 16c,d, respectively, only with the top view, but the overlap of the shifted elements can be clearly observed. Figure 16e shows the CFSS #4, which has only one metal layer.

Measurements were carried out using an Agilent E5071C Vector Network Analyzer, two SAS-571 double ridge horn antennas (frequency range from 700 MHz to 18 GHz, and linearly polarised) and a measurement window with pyramidal radiation-absorbent material surrounding it (Figure 17). The two horn antennas were placed facing each other at a fixed position, with a distance of 160 cm to ensure that the transmitter and receiver antennas are in the far-field regions. The wave to the FSSs is considered to be at normal ( $\theta = 0^\circ$ ) and oblique ( $\theta =$  up to  $40^\circ$ ) incidence, and the latter angle is limited by the absorbers around the measurement window.

#### 4.1 | CFSS results

The numerical and measured results for the CFSS #1 for the TE and TM polarisation are presented in Figure 18. The behaviour of the structure for normal ( $\theta = 0^\circ$ ) and oblique ( $\theta \neq 0^\circ$ ) incidence are depicted. There are two transmission maxima ( $f_{p1}$  and  $f_{p2}$ ) and one transmission zero ( $f_z$ ) as predicted in the previous section for the FSS which is perfectly complemented and they are controlled by the elements'

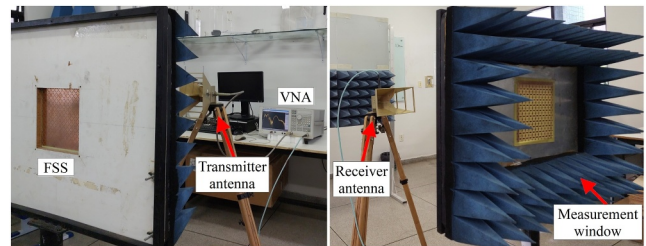


**FIGURE 17** Measurement setup.

dimensions. The CFSS was designed to operate at  $f_{p1} = 2.6$  GHz and  $f_{p2} = 6.2$  GHz. For the TE polarisation (Figure 18a), the measured transmission maxima are 2.63 GHz ( $-1.81$  dB) and 6.37 GHz ( $-2.36$  dB) with a transmission zero at 4.16 GHz ( $-25.78$  dB), showing a good agreement with those obtained numerically,  $f_{p1} = 2.58$  GHz ( $-1.23$  dB),  $f_{p2} = 6.26$  GHz ( $-2.11$  dB) and  $f_z = 4.18$  GHz ( $-41.74$  dB). The frequency response of the structure in this polarisation is stable to the variation of incidence angle. The CFSS #1 is symmetrical, which means the results for the TM polarisation are similar to the ones from the TE polarisation. For the TM polarisation (Figure 18b), the simulated and measured resonant frequencies are  $f_{p1} = 2.58$  GHz ( $-1.23$  dB) and 2.67 GHz ( $-2.36$  dB),  $f_{p2} = 6.22$  GHz ( $-2.11$  dB) and 6.32 GHz ( $-2.98$  dB), and  $f_z = 4.05$  GHz ( $-32.63$  dB) and 4.28 GHz ( $-28.75$  dB), respectively. Note that in this polarisation, the structure is relatively stable to the normal and off-normal

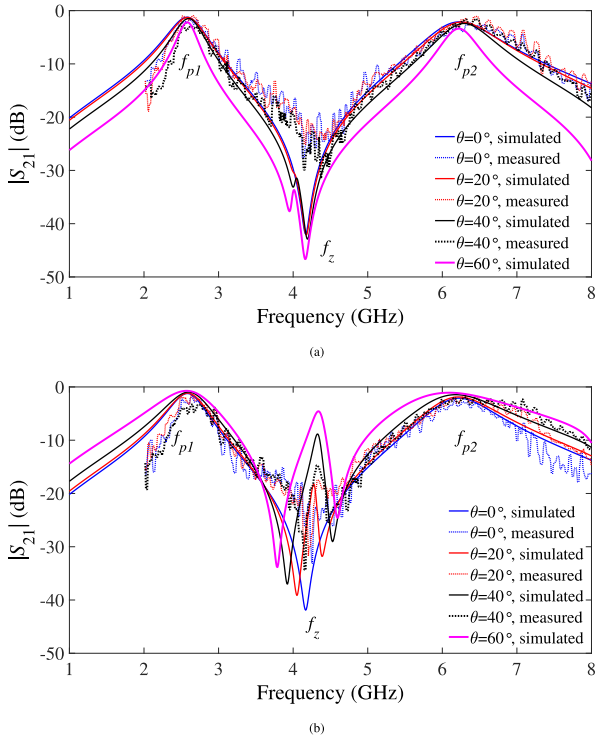


**FIGURE 18** Simulated and measured results for (a) TE and (b) TM polarisation of CFSS #1.

incidence at the transmission maxima, although a resonance arises in the transmission zero at 4.28 GHz from simulated results. This effect occurs because the E-field starts to probe the broken intrinsic symmetry of the structure causing the destructive interference of scattered fields. The transparency window becomes stronger when  $\theta$  increases, thus two transmission zeros appear. Based on this phenomenon, the offset of the elements is analysed to understand how breaking the symmetry of complementary structures can lead to another transmission maximum.

## 4.2 | Offset CFSS results

Vertical and diagonal offsets were implemented to allow a transparency window between the two original transmission maxima. The simulated and measured S-parameter spectra for these structures are shown in Figures 19 and 20, exhibiting a third passband obtained by the EIT-like effect.

Figure 19 shows the results of the CFSS with a vertical offset of its elements (CFSS #2). Three transmission maxima are observed in the TE polarisation, two as seen in CFSS #1, and the third is due to the offset. The simulated transmission maxima are  $f_{p1} = 2.45$  GHz ( $-1.44$  dB),  $f_o = 4.3$  GHz ( $-2.7$  dB) and  $f_{p2} = 6.28$  GHz ( $-2.58$  dB), and the measured ones are  $f_{p1} = 2.49$  GHz ( $-1.65$  dB),  $f_o = 4.33$  GHz ( $-1.74$  dB) and  $f_{p2} = 6.48$  GHz ( $-3.4$  dB) (Figure 19a), with a maximum difference of 1.6%, 0.69% and 3.08%, respectively. For the TM polarisation (Figure 19b), the frequency characteristics remain similar to the one seen for CFSS #1 with simulated and

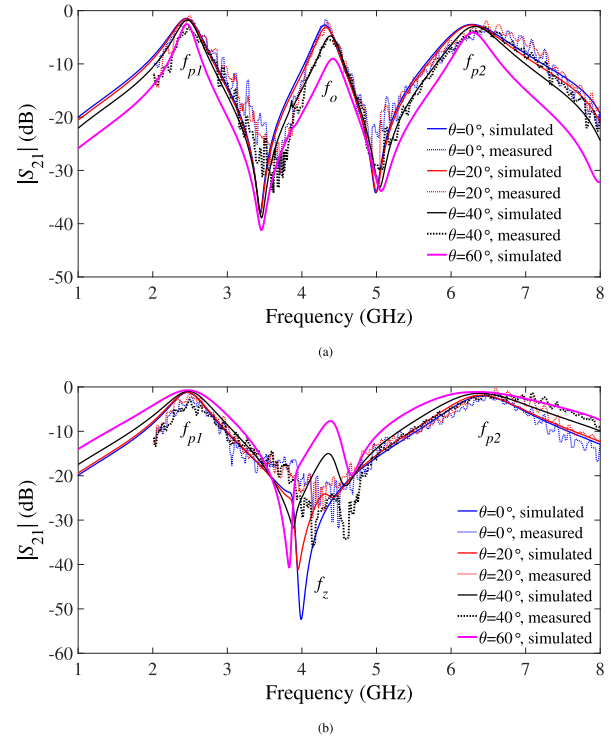


**FIGURE 19** Simulated and measured results for (a) TE and (b) TM polarisation of CFSS #2.

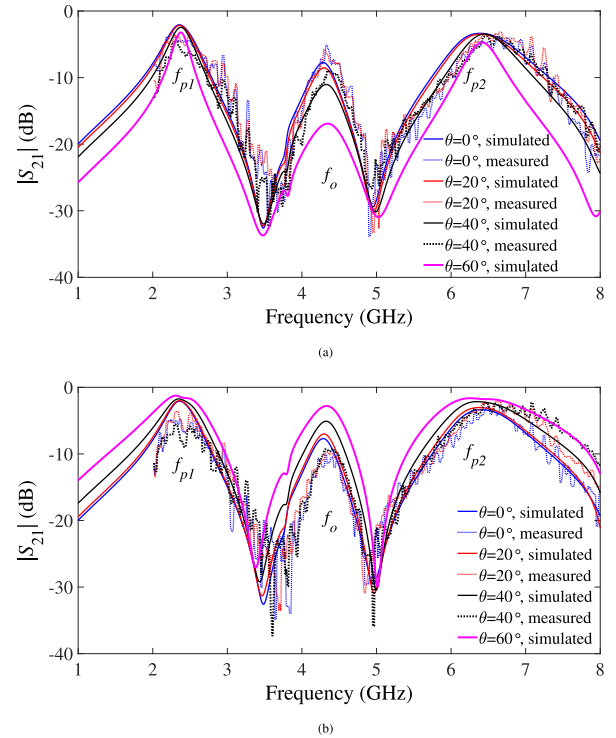


**FIGURE 20** Simulated and measured results for (a) TE and (b) TM polarisation of CFSS #3.

measured resonant frequencies  $f_{p1} = 2.47$  GHz ( $-1.24$  dB) and 2.52 GHz ( $-2.29$  dB), and  $f_{p2} = 6.44$  GHz ( $-2.02$  dB) and 6.52 GHz ( $-2.47$  dB), with a maximum difference of 1.98% and 1.23%, respectively. Thus, the offset in the CFSS can work

as another parameter to control the frequency response by modifying the electromagnetic coupling level.

The CFSS #3 has a diagonal offset of both elements as indicated in Figure 10, resulting in three passbands for both TE and TM polarisations as shown in Figure 20a,b, respectively. This configuration shows a behaviour similar to that of CFSS #2, where the offset between the elements acts directly as the coupling level. The shift of the elements produces the third passband where originally there was a transmission zero. The transmission maxima in the TE polarisation are  $f_{p1} = 2.36$  GHz ( $-2.07$  dB),  $f_o = 4.28$  GHz ( $-7.74$  dB) and  $f_{p2} = 6.39$  GHz ( $-3.35$  dB), simulated, and  $f_{p1} = 2.29$  GHz ( $-3.2$  dB),  $f_o = 4.36$  GHz ( $-5.14$  dB) and  $f_{p2} = 6.66$  GHz ( $-4.29$  dB), measured. Different from CFSS #1 and #2, this configuration presents the third passband in the TM polarisation, where the resonant frequencies of the simulated and experimental characterisation are  $f_{p1} = 2.36$  GHz ( $-2.08$  dB) and 2.26 GHz ( $-4.83$  dB),  $f_o = 4.28$  GHz ( $-7.69$  dB) and 4.37 GHz ( $-10.18$  dB), and  $f_{p2} = 6.41$  GHz ( $-3.36$  dB) and 6.49 GHz ( $-2.88$  dB), respectively. Note that compared with Figure 8b, the higher insertion loss observed in Figure 20a,b is due to the fact that FR4 is a relatively lossy material with a loss tangent of only 0.025.

### 4.3 | Single-layered quasi-CFSS results

The results of the fourth proposed complementary-based structure are shown in Figure 21. CFSS #4 was fabricated using the dimensions of Case #7 (Table 1), and its characterisation also considered normal and oblique incidence with  $\theta$  up to  $20^\circ$ . For the TE polarisation, the two transmission maxima at 2.5 GHz ( $-0.38$  dB) and 6.7 GHz ( $-1.9$  dB), numerical, and 2.66 GHz ( $-0.43$  dB) and 6.83 GHz ( $-1.61$  dB), experimental, are the same for all incidence angles. A Fano resonance [34, 35] starts arising when  $\theta = 20^\circ$ , but it does not interfere with the bandwidths. When in the TM polarisation, transmission maxima are found to be basically the same as in the TE polarisation due to its symmetry, with simulated and measured resonances  $f_{p1} = 2.5$  GHz ( $-0.39$  dB) and 2.67 GHz ( $-0.71$  dB), and  $f_{p2} = 6.7$  GHz ( $-1.91$  dB) and 6.7 GHz ( $-0.54$  dB), respectively. The Fano resonance is observed at  $\theta = 10^\circ$ , and its amplitude increases as the oblique angle increases. Note that this structure shows a similar behaviour as previous complementary FSSs, although it only uses one metal layer, and the coupling between the elements induces a Fano resonance at low oblique angles.

### 4.4 | Performance assessment

Transmission measurement results confirm that a multi-band response is achieved by stacking complementary elements on double metal layer substrates or using quasi-complementary elements on a single metal layer substrate. Furthermore, if the offset of the elements is applied, a transparency window appears where initially it was a transmission null. Table 2

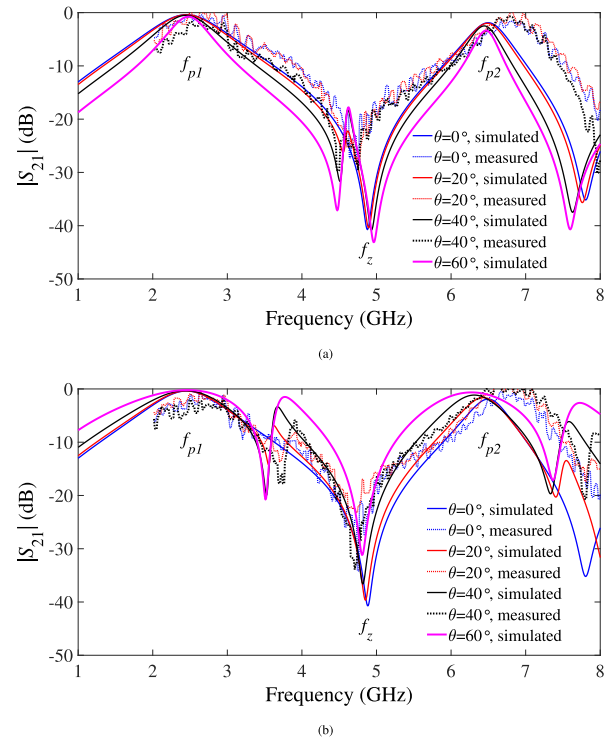


**FIGURE 21** Simulated and measured results for (a) TE and (b) TM polarisation of CFSS #4.

summarises the frequency response of each proposed structure in terms of number of passbands and stopbands for TE and TM polarisations and approximated value of the transmission and reflection bandwidths (BW)s. CFSS #1 and CFSS #4 have the same number of bands for both polarisations, with two passbands and one stopband, but the bandwidths exhibit a complementary behaviour due to the resized elements in CFSS #4 to dovetail. Depending on the offset applied, the FSS can exhibit two passbands and one stopband, or three passbands and two stopbands ( $f_{z1}$  and  $f_{z2}$ ). CFSS #2 shows similar characteristics to CFSS #1 and CFSS #4 in the TM polarisation. CFSS #3 presents the same response for both polarisations, which is similar to CFSS #2 in the TE polarisation, with narrower BW.

The characteristics of our proposed structures are compared with previously related works in Table 3, which include their type of configuration, number of bands, frequencies of operation, unit cell dimensions, polarisation sensitivity, angular stability (AS), RFD and transmission loss (TL). It can be observed that the proposed multi-band FSSs are more compact in terms of number of layers used and the size of the unit cell in order of wavelength of the lower band in free space. Depending on the configuration for the complementary structure, it can be sensitive or insensitive to the polarisation of the incident wave and exhibits dual- and/or triple-bands of operations while keeping the original transmission maxima. In all configurations, the proposed CFSSs showed good angular stability for oblique incidence up to  $60^\circ$  with maximum RFD of 0.35% from  $\theta = 0^\circ$ – $60^\circ$  (for the original CFSS).



**TABLE 2** Summarised frequency response for TE and TM polarisation of the proposed structures with  $-10$ -dB bandwidth.

Structure	NPB <sub>TE</sub>	NSB <sub>TE</sub>	NPB <sub>TM</sub>	NSB <sub>TM</sub>	BW <sub>p1</sub> (GHz)	BW <sub>p2</sub> (GHz)	BW <sub>o</sub> (GHz)	BW <sub>z</sub> (GHz)	BW <sub>z1</sub> (GHz)	BW <sub>z2</sub> (GHz)
CFSS #1	2	1	2	1	1.21	2.08	–	2.27	–	–
CFSS #2	3	2	2	1	0.97/1.13	1.65/2.11	0.56	2.56	1.16	1.08
CFSS #3	3	2	3	2	0.92	1.56	0.32	–	1.33	1.31
CFSS #4	2	1	2	1	2.41	1.21	–	2.21	–	–

Abbreviations: NPB, number of pass-bands; NSB, number of stop-bands.

**TABLE 3** Comparison of proposed multi-band FSS with other reported ones.

Ref.	Configuration	No. of bands	Frequencies (GHz)	Unit cell size	PI	AS ( $\theta_{\max}$ )	RFD (%)	TL (dB) <sup>a</sup>
[13]	1-metal and 1-dielectric	2	11.13 and 13.29	$0.27\lambda \times 0.27\lambda$	No	$60^\circ$	0.50	<1
[14]	2-metal and 1-dielectric	3	2.4, 5.2 and 5.9	$0.20\lambda \times 0.20\lambda$	Yes	$60^\circ$	1.60	<2
[17]	3-metal and 2-dielectric	2 and 1	7.28 and 26.94, and 11.39	$0.08\lambda \times 0.24\lambda$	No	$60^\circ$	NA	<2
[18]	3-metal and 2-dielectric	3	20.9 and 29.9 and 38.5	$0.15\lambda \times 0.15\lambda$	Yes	$60^\circ$	1.00	<1
[20]	3-metal and 2-dielectric	2	2.5 and 5.5	$0.10\lambda \times 0.10\lambda$	No	$45^\circ$	NA	<3
[21]	1-metal and 1-dielectric	3	8.11, 9.81 and 11	$0.55\lambda \times 0.55\lambda$	Yes	$60^\circ$	NA	<4
[22]	1-metal and 1-dielectric	2	2.42 and 5.11	$0.18\lambda \times 0.18\lambda$	Yes	$45^\circ$	2	<5
[23]	2-metal and 1-dielectric	2	From 1.3 to 1.64 and from 2.34 to 2.9	$0.048\lambda \times 0.048\lambda$	Yes	$60^\circ$	NA	<5
This work	2/1-metal and 1-dielectric	2 and/or 3	2.6, 4.2 and 6.2	$0.14\lambda \times 0.14\lambda$	Dual	$60^\circ$	0.35	<8

Abbreviations: NA, RFD value is not available; PI, polarization insensitive.

<sup>a</sup>Transmission loss estimated from figures in the references.

## 5 | CONCLUSION

Multi-band closely coupled-complementary based FSSs with dual- and triple-passbands response are proposed in this paper that can be applied to increase the capability of multi-frequency antennas in satellite or other communication systems. The proposed CFSSs consist of a stacked periodic array of four-arms star geometry patch-type element and its complementary one on a single dielectric substrate. Parametric analyses and offsets were used to evaluate the coupling between these elements, and how the break of symmetry can generate a transmission window between the original transmission maxima. CFSS #1 and CFSS #4 have their elements centred within the unit cell, which can create two transmission maxima ( $f_p$ ) and a transmission zero between them. Using CFSS #1 as reference, the operating frequencies are around  $f_{p1} = 2.6$  GHz,  $f_z = 4.2$  GHz (that can become a transmission maxima), and  $f_{p2} = 6.2$  GHz. Vertical (CFSS #2) and diagonal (CFSS #3) offsets were implemented that created a third  $f_p$ , where the original was a transmission zero, by inducing an EIT-like effect. CFSS #2 presented three  $f_p$  in the TE polarisation and two  $f_p$  in the TM polarisation, showing to be polarisation dependent. CFSS #3 showed three  $f_p$  in both polarisations, and the third one appeared again at the previous transmission zero frequency. CFSS #1, #3 and #4 presented polarisation-insensitive performance. All structures were fabricated and characterised; the experimental results closely follow the ones obtained from the simulations. The designed structures showed stable behaviour for different incident angles for both

TE and TM polarisations. In comparison to related published works, this design approach exhibits dual and/or triple-bands of operation with the capability of being polarisation insensitive or sensitive and results in a compact single-substrate-layer configuration.

## AUTHOR CONTRIBUTIONS

**Deisy F. Mamedes:** Data curation; methodology; formal analysis; investigation; visualization; writing – original draft.

**Jens Bornemann:** Supervision; funding acquisition; resources; writing – review & editing. **Alfredo Gomes Neto:** Resources; validation. **Sérgio L. M. Sales Filho:** Validation.

## CONFLICT OF INTEREST STATEMENT

The authors declare no conflicts of interest.

## DATA AVAILABILITY STATEMENT

All the data in this manuscript is provided in this publication.

## ORCID

Deisy F. Mamedes  <https://orcid.org/0000-0002-8062-0722>

## REFERENCES

- Munk, B.A.: Element Types: A Comparison, pp. 50–51. Wiley (2000)
- Anwar, R.S., Mao, L., Ning, H.: Frequency selective surfaces: a review. *Appl. Sci.* 8(9), 1689 (2018). <https://doi.org/10.3390/app8091689>
- Su, Y.L., et al.: Dichroic sub-reflector for wide band techniques for single offset antenna. In: 2018 48th European Microwave Conference (EuMC), pp. 268–271 (2018)



4. Vásquez-Peralvo, J.A., et al.: Inductive frequency selective surface: an application for dichroic sub-reflectors. *IEEE Access* 8, 22721–22732 (2020). <https://doi.org/10.1109/ACCESS.2020.2970271>
5. Yang, C., Liu, P., Zhu, X.: Circularly polarized microstrip patch antenna array based on FSS polarization converter. In: 2019 International Symposium on Antennas and Propagation (ISAP), pp. 1–3 (2019)
6. Mamedes, D.F., Bornemann, J., Neto, A.G.: Linear-to-Circular polarization converter based on four-arms star FSS at 5.2 GHz for 5G applications. In: 2022 16th European Conference on Antennas and Propagation (EuCAP), pp. 1–4 (2022)
7. Pazokian, M., Komjani, N., Karimipour, M.: Broadband RCS reduction of microstrip antenna using coding frequency selective surface. *IEEE Antenn. Wireless Propag. Lett.* 17(8), 1382–1385 (2018). <https://doi.org/10.1109/LAWP.2018.2846613>
8. Baskey, H.B., Akhtar, M.J.: Design of flexible hybrid nanocomposite structure based on frequency selective surface for wideband radar cross section reduction. *IEEE Trans. Microw. Theor. Tech.* 65(6), 2019–2029 (2017). <https://doi.org/10.1109/TMTT.2017.2655045>
9. Huang, Z., et al.: Tapered resistive sheets and FSS absorber loading for the wideband RCS reduction of the elliptic surface at TM polarization. *IEEE Trans. Antenn. Propag.* 71(7), 6191–6195 (2023). <https://doi.org/10.1109/TAP.2023.3265462>
10. Xie, D., et al.: A wideband absorber with a multiresonant gridded-square FSS for antenna RCS reduction. *IEEE Antenn. Wireless Propag. Lett.* 16, 629–632 (2017). <https://doi.org/10.1109/LAWP.2016.2594213>
11. Wang, H., et al.: Design of a self-complementary frequency selective surface with multi-band polarization separation characteristic. *IEEE Access* 7, 36788–36799 (2019). <https://doi.org/10.1109/ACCESS.2019.2905416>
12. Liu, X., et al.: Extension of Babinet principle to complementary metallic elements on the interface of different substrates. *IEEE Microw. Wireless Compon. Lett.* 32(10), 1151–1154 (2022). <https://doi.org/10.1109/LMWC.2022.3173794>
13. Liu, N., et al.: An angular stable dual-band frequency selective surface with closely spaced resonances. *Prog. Electromagnetics Res. Lett.* 70, 1–6 (2017). <https://doi.org/10.2528/PIER17070302>
14. Karahan, M., Aksoy, E.: Design and analysis of angular stable antipodal F-type frequency selective surface with multi-band characteristics. *Int. J. RF Microw. Computer-Aided Eng.* 30(12), e22466 (2020). <https://doi.org/10.1002/mmce.22466>
15. Zhou, H., et al.: Dual band frequency selective surface based on circular aperture-coupled patches. *Microw. Opt. Technol. Lett.* 53(8), 1784–1786 (2011). <https://doi.org/10.1002/mop.26102>
16. Yan, M., et al.: A miniaturized dual-band FSS with second-order response and large band separation. *IEEE Antenn. Wireless Propag. Lett.* 14, 1602–1605 (2015). <https://doi.org/10.1109/LAWP.2015.2413942>
17. Wang, H., et al.: Design and analysis of miniaturized low profile and second-order multi-band polarization selective surface for multipath communication application. *IEEE Access* 7, 13455–13467 (2019). <https://doi.org/10.1109/ACCESS.2019.2894013>
18. He, Z., et al.: A tri-band highly selective passband frequency selective surface based on multi-layer coupling. In: 2021 IEEE International Symposium on Antennas and Propagation and USNC-URSI Radio Science Meeting (APS/URSI), pp. 1693–1694 (2021)
19. Yan, M., et al.: A tri-band, highly selective, bandpass FSS using cascaded multilayer loop arrays. *IEEE Trans. Antenn. Propag.* 64(5), 2046–2049 (2016). <https://doi.org/10.1109/TAP.2016.2536175>
20. Chatterjee, A., Parui, S.K.: A triple-layer dual-bandpass frequency selective surface of third order response with equivalent circuit analysis. *Int. J. RF Microw. Computer-Aided Eng.* 30(2), e22047 (2020). <https://doi.org/10.1002/mmce.22047>
21. Mahaveer, U., et al.: A tri-band frequency-selective surface. *J. Electromagn. Waves Appl.* 35(7), 861–873 (2021). <https://doi.org/10.1080/09205071.2020.1865206>
22. Neto, A.G., et al.: Dual-band band-pass frequency selective surface based on the Matryoshka geometry with angular stability and polarization independence. In: 2020 14th European Conference on Antennas and Propagation (EuCAP), pp. 1–4 (2020)
23. Ma, Y.H., et al.: Design of dual-band frequency-selective surfaces with independent tunability. *IEEE Trans. Antenn. Propag.* 70(12), 12381–12386 (2022). <https://doi.org/10.1109/TAP.2022.3209263>
24. Hu, X.D., et al.: A novel dual-band frequency selective surface (FSS). In: 2009 Asia Pacific Microwave Conference, pp. 1227–1230 (2009)
25. Coomar, S., Mondal, S., Sanyal, R.: Compact, flexible and highly selective wideband complementary FSS with high angular stability. *Int. J. Microwave Wireless Tech.* 14(10), 1298–1314 (2022). <https://doi.org/10.1017/s1759078721001707>
26. Kim, D., et al.: Characterization of nematic liquid crystal dielectric properties using complementary FSSs featuring electrically small cell gaps across a wide sub-THz range. *IEEE Trans. Antenn. Propag.* 72(2), 2019–2024 (2024). <https://doi.org/10.1109/TAP.2023.3344274>
27. Mamedes, D.F., Bornemann, J.: Using an equivalent-circuit model to design ultra-wide band-stop frequency-selective surface for 5G mm-wave applications. *IEEE Open J. Antennas Propagation* 3, 948–957 (2022). <https://doi.org/10.1109/OJAP.2022.3198290>
28. Munk, B.A.: *Frequency Selective Surfaces: Theory and Design*. John Wiley & Sons (2005)
29. Kiani, G.I., et al.: Cross-dipole bandpass frequency selective surface for energy-saving glass used in buildings. *IEEE Trans. Antenn. Propag.* 59(2), 520–525 (2011). <https://doi.org/10.1109/TAP.2010.2096382>
30. Costa, F., Monorchio, A., Manara, G.: Efficient analysis of frequency-selective surfaces by a simple equivalent-circuit model. *IEEE Antenn. Propag. Mag.* 54(4), 35–48 (2012). <https://doi.org/10.1109/MAP.2012.6309153>
31. Hu, X.D., et al.: A miniaturized dual-band frequency selective surface (FSS) with closed loop and its complementary pattern. *IEEE Antenn. Wireless Propag. Lett.* 8, 1374–1377 (2009). <https://doi.org/10.1109/LAWP.2009.2039110>
32. Krushna Kanth, V., Raghavan, S.: Equivalent circuit analysis of complementary FSS for selective EM shielding. In: 2018 15th International Conference on ElectroMagnetic Interference & Compatibility (INCEMIC), pp. 1–4 (2018)
33. Kanth, V.K., Raghavan, S.: Complementary frequency selective surface array optimization using equivalent circuit model. In: 2017 IEEE MTT-S International Microwave and RF Conference (IMaRC), pp. 1–4 (2017)
34. Komarov, V.V., et al.: Fano-resonant frequency-selective surface with cross-shaped apertures. *IEEE Microw. Wireless Compon. Lett.* 29(12), 775–778 (2019). <https://doi.org/10.1109/LMWC.2019.2948987>
35. Wu, C., et al.: Spectrally selective chiral silicon metasurfaces based on infrared Fano resonances. *Nat. Commun.* 5(1), 1–9 (2014). <https://doi.org/10.1038/ncomms4892>

**How to cite this article:** F. Mamedes, D., et al.: Dual- and triple-passband coupled-complementary FSSs based on the four-arms star geometry. *IET Microw. Antennas Propag.* 1–13 (2024). <https://doi.org/10.1049/mia2.12477>